

Simulation of the first two microseconds of an Ar CCP cold plasma discharge by the PIC-MCC method

Original

Simulation of the first two microseconds of an Ar CCP cold plasma discharge by the PIC-MCC method / Mandracci, Pietro. - In: PLASMA. - ISSN 2571-6182. - ELETTRONICO. - 5:3(2022), pp. 366-383. [10.3390/plasma5030028]

Availability:

This version is available at: 11583/2971438 since: 2022-09-19T11:33:51Z

Publisher:

MDPI

Published

DOI:10.3390/plasma5030028

Terms of use:

This article is made available under terms and conditions as specified in the corresponding bibliographic description in the repository

Publisher copyright

(Article begins on next page)

Article

Simulation of the First Two Microseconds of an Ar CCP Cold Plasma Discharge by the PIC-MCC Method

Pietro Mandracci 

Department of Applied Science and Technology, Politecnico di Torino, Corso Duca degli Abruzzi 24, 10129 Turin, Italy; pietro.mandracci@polito.it

Abstract: Most simulations of capacitively coupled radiofrequency cold-plasma discharges (RF-CCP) are focused on the steady state, but the initial discharge time is important for understanding the ignition process and the behavior of pulsed discharges. In this work, the time evolution of an RF-CCP Ar discharge was simulated, considering a pressure of 66.6 Pa, a distance between the electrodes of 20 mm, and RF (13.56 MHz) bias amplitudes in range 100–400 V, and the discharge evolution was observed for the first 2 μ s. A 1d3v (1 dimension for particle positions and 3 dimensions for particle velocities) electrostatic particle in cell with monte-carlo collisions (PIC-MCC) model was used, with separated particle weights for electrons and ions that varied with the particle density. During the simulations, the time evolution of the electron density, mean electron energy, Debye length, Debye number, and plasma frequency were observed. The spatial distribution of electric potential and the electron energy distribution function were also monitored. A transition between two regimes was observed; the first was characterized by strong oscillation of the mean electron energy and an exponential increase of the mean plasma density with time, while in the second the mean electron energy was lower, and the plasma density increased linearly. The time required for the transition between the two regimes increased as the RF amplitude was raised from 100 to 250 V, then decreased with a further increase of the RF amplitude to 300 and 350 V.



Citation: Mandracci, P. Simulation of the First Two Microseconds of an Ar CCP Cold Plasma Discharge by the PIC-MCC Method. *Plasma* **2022**, *5*, 366–383. <https://doi.org/10.3390/plasma5030028>

Academic Editor: Andrey Starikovskiy

Received: 15 August 2022

Accepted: 9 September 2022

Published: 16 September 2022

Publisher's Note: MDPI stays neutral with regard to jurisdictional claims in published maps and institutional affiliations.



Copyright: © 2022 by the author. Licensee MDPI, Basel, Switzerland. This article is an open access article distributed under the terms and conditions of the Creative Commons Attribution (CC BY) license (<https://creativecommons.org/licenses/by/4.0/>).

Keywords: PIC-MCC; cold plasma; Argon; capacitively coupled discharge; time evolution

1. Introduction

Capacitively coupled cold-plasma discharges activated by radiofrequency (RF-CCP) [1] are of widespread use for thin-film deposition and surface modification processes [2] in a wide range of applications, including microelectronics [3], photovoltaics [4], energy-saving materials [5], pollution control [6], as well as biological applications [7–9]. Among RF-CCP discharges, those working at low pressure (lower than atmospheric) have been in use for a longer time, despite their requirement for expensive vacuum systems, because they require less power to be activated compared with atmospheric pressure discharges, and are less sensitive to contamination by atmospheric gases. [1].

Due to their importance, considerable experimental and theoretical work has been carried out to improve the understanding of the physico-chemical processes involved in low-pressure RF-CCP discharges. However, most of the experimental and simulation work has focused on the characteristics of the steady state when the plasma parameters have reached a stationary condition, as this is the regime in which the technological applications of the plasma discharge, such as thin-film deposition or surface etching, are more controllable. However, the initial part of the process, which is required for the onset of a stable discharge, is important for understanding the plasma ignition, as well as for the study of pulsed discharges. In fact, several experimental and theoretical works have been published in recent years to describe some aspects of the evolution with time of plasma parameters in different types of capacitively coupled RF discharges. These studies have particularly focused on pulsed discharges, and most of them have dealt with a time scale

using microsecond [10–12], millisecond [13], or even second [14] resolution, while less information can be found relating to time evolution with nanosecond resolution [15,16]. However, according to the results obtained in this work, transition between different discharge mechanisms can take place at the very beginning of the discharge, in a time lower than one microsecond.

In this work, a low-pressure capacitively coupled discharge in a parallel-plate reactor was simulated, starting from the first activation of the electric bias on the electrodes and tracking the discharge evolution through time for 2 μ s. A 1d3v electrostatic PIC-MCC model was used, with particle weights different for electrons and ions and which varied as the numbers of electrons and ions increased, allowing the number of superparticles to remain in a limited range, even with dramatic changes in the number of real particles. The time evolution of several quantities was followed during the simulation, including the mean electron energy, the electron density n_e , the Debye length λ_D , the Debye number N_D and the plasma frequency ν_p . The spatial distribution of the electric potential inside the discharge was also monitored, as well as the electron energy distribution function (EEDF).

2. Materials and Methods

2.1. Physical Characteristics of the Simulated Discharge

In this work, a parallel-plate, radio-frequency, low-pressure Ar discharge was simulated, using the physical parameters showed in Table 1. The gas temperature T_{gas} and pressure p were fixed at 300 K and 66.6 Pa (0.5 Torr), respectively, and the distance d between the two planar electrodes set to 20 mm, providing a pd value of 1.33 Pa m (1 Torr cm). The electrodes were of square shape and their lateral length was chosen to provide a sufficiently large plasma volume to obtain at least some hundreds of free electrons and ions inside the discharge at the beginning of the simulation. A radiofrequency sinusoidal signal with a frequency of 13.56 MHz was used to simulate the electric bias applied between the electrodes, and seven values of the signal amplitude were compared: 100, 150, 200, 250, 300, 350, and 400 V. The initial phase of the sinusoidal signal was fixed at 0 degrees, which means that at $t = 0$ s the potential difference between the electrodes was 0 V.

Table 1. Physical characteristics of the simulated discharge.

Quantity	Symbol	Value	Unit
Electrodes lateral length	l	250	mm
Distance between the electrodes	d	20	mm
Plasma volume	$V_{pla} = l^2 \cdot d$	1.25×10^{-3}	m^3
Gas temperature	T_{gas}	300	K
Gas pressure	p	66.6	Pa
Gas molecule density	n_{gas}	1.6×10^{22}	m^{-3}
Electric bias peak value	ΔV_{max}	100	V
		150	
		200	
		250	
		300	
		350	
		400	
Electric bias frequency	ν_{RF}	13.56	MHz
Electric bias period	$\tau_{RF} = 1/\nu_{RF}$	73.75	ns
Electric bias starting phase	φ_0	0	$^\circ$

2.2. Details of the Simulation Process

The simulations were carried out using CCPLA software (version 0.2.0, Pietro Mandracci, Turin, Italy) which is freely available online. The software is designed to simulate a gas discharge in the volume comprised between two parallel square electrodes, between which a DC or RF signal is applied, and inside which a gas or gas mixture at low pressure is confined. The details of the CCPLA software are reported in Appendix A.

The main simulation parameters are reported in Table 2. An initial ionization degree of 4×10^{-17} was considered, which is consistent with positive ion density at atmospheric pressure of about 10^9 m^{-3} , usually reported for air in a closed environment [17,18]. Considering the given Ar gas pressure of 66.6 Pa, this value provides an initial electron density of $6.4 \times 10^5 \text{ m}^{-3}$, and an initial number of computational particles of about 800 for each particle type (electrons and Ar^+ ions). The starting positions of the electrons and ions in the plasma volume were determined randomly, following uniform distributions along the x, y, and z axes. The particle speeds were randomly extracted according to the Maxwell–Boltzmann distribution, with a temperature equal to the one of the neutral Ar atoms (300 K), while the initial velocity directions were randomly determined with uniform distribution of the solid angle.

Table 2. Simulation parameters.

Quantity	Symbol	Value	Unit
Starting ionization degree	$\alpha(0)$	4×10^{-17}	
Starting electron density	$n_e(0) = n_{\text{gas}} \cdot \alpha(0)$	6.41×10^5	m^{-3}
Simulation time step	Δt	10	ps
Time between data acquisitions	Δt_{output}	1	ns
Overall simulated time	Δt_{total}	2	μs
Maximum number of computational particles	N_e^{max}	5×10^4	
Number of PIC cells (1D)	N_z	300	
Dimension of a PIC cell	Δz	66.67	μm

The number density of the neutral Ar atoms was considered constant throughout the simulation time, neglecting its variation due to the transformation of neutral atoms in ions provided by the ionization processes. This approximation is justified by the maximum electron density obtained during the simulation, which was always lower than 10^{15} m^{-3} (see Section 3.1), seven orders of magnitude lower than the neutral density $n_{\text{gas}} \sim 10^{22} \text{ m}^{-3}$.

A constant time step $\Delta t = 10 \text{ ps}$ was chosen, and the space between the electrodes was divided into 300 one-dimensional cells of size $\Delta z = 66.7 \mu\text{m}$. These values were chosen to satisfy the usual requirements for stability and accuracy of the PIC simulation scheme [19]:

- the RF period was divided in 7375 time steps, providing good resolution of the RF behavior;
- the probability of obtaining a collision during a time step (given by Equation (A1)) was lower than 0.05, providing a negligible probability of multiple collisions during a time step;
- considering that the plasma frequency was always $\nu_p < 2 \times 10^9 \text{ s}^{-1}$ during all simulation runs (see Section 3.5), the condition $\nu_p \Delta t < 0.1$ was always satisfied;
- considering that the minimum value of the Debye length was about $200 \mu\text{m}$ (see Section 3.3), the condition $\Delta z < \lambda_D$ was always satisfied;
- the particles were not able to travel a distance greater than Δz during a time step; the speed required to do so is $v = \Delta z / \Delta t = 6.67 \times 10^6 \text{ m s}^{-1}$, which for an electron requires a kinetic energy of about 126 keV, much higher than the electron energy in the *EEDF* tails (see Section 3.7).

Certain boundary conditions were used by the Poisson solver for the electric potential calculation; the grounded electrode positioned at $z = 20$ mm was considered at a fixed potential of zero volts, while the potential at the biased electrode positioned at $z = 0$ mm was considered equal to the value of the RF amplitude at the given simulation time. The electrons and ions were removed from the discharge when they reached one of the electrodes (z equal to 0 or 20 mm), while if they reached one of the electrode borders (x or y equal to 0 or 250 mm) they were made to re-enter on the opposite side. The emission of secondary electrons from the electrodes was not included in the model.

The simulation model included elastic, excitation, and ionization collisions for electrons, and elastic and charge exchange collisions for ions, as shown in Table 3. The Ar atoms were considered at rest for the electron–atom collisions, while for collisions between an ion and an atom both were considered moving and the collision was simulated inside the center of mass frame of reference (COMFOR). More details of the collision processes are given in Appendix A.

Table 3. Collision processes considered in the simulation.

Collision Type	First Particle	Second Particle	Ref.
Elastic	Electron	Ar atom	[20]
Excitation	Electron	Ar atom	[20]
Ionization	Electron	Ar atom	[20]
Elastic	Ar ⁺ ion	Ar atom	[21]
Charge exchange	Ar ⁺ ion	Ar atom	[21]

The simulations required between four and five hours to be completed, run on a PC equipped with an octacore CPU (AMD Ryzen 7 4800 H) using a single core only at a clock frequency of 4.2 GHz for the numerical computation cycles, while more cores were used to manage the software GUI and the runtime plots.

2.3. Calculated Plasma Parameters

The time evolution of various physical quantities was considered during the simulation runs, i.e.: electron density n_e , electron mean energy $\langle E_e \rangle$, Debye length λ_D and number N_D , and plasma frequency ν_p . The electron density and the electron mean energy were simulated directly by the CCPLA software during the simulation runs, and the other three quantities were calculated as described in Appendix B. The spatial distribution of the electric potential along the direction normal to the electrodes (z axis) was also monitored, and selected samples are reported in Section 3.6. The electron energy distribution function (EEDF) was monitored, and samples acquired at different simulation times are reported in Section 3.7.

3. Results

3.1. Electron Density

The time evolution of the electron density, for electric bias peak values between 100 and 400 V, is shown in Figure 1, using (a) linear and (b) semilogarithmic scales. Zoomed graphs of (c) the first 100 ns in linear scale and (d) the 700–1500 ns range in semilogarithmic scale are also provided. For bias voltage values in the 150–350 V range, a quite abrupt change between two different regimes was observed, first up to about 750–1250 ns, depending on the bias voltage, and a second after about 1–1.5 μ s, with a transition region between the two regimes. For the 100 V peak bias value there was no transition, and the first regime was observed up to 2 μ s of simulated time. For the 400 V peak bias, contrastingly, the mean value of electron density decreased with time, and after about 750 ns it dropped to zero, meaning that no more electrons were present in the simulated discharge.

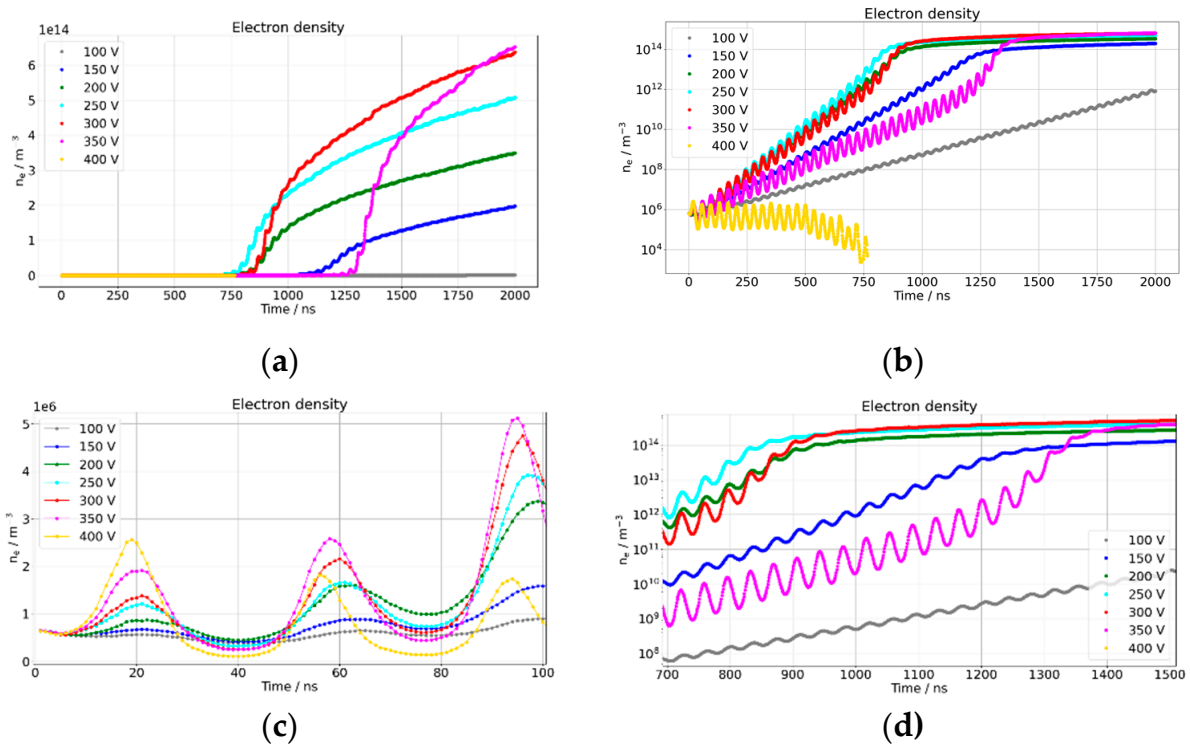


Figure 1. Time evolution of the electron density during the simulation for different values of the peak bias voltage: (a) Linear scale; (b) semilogarithmic scale; (c) zoom of region 0–100 ns in linear scale; and (d) zoom of region 700–1500 ns in semilogarithmic scale.

In the first regime, for the 100–350 V peak bias voltages, the electron density was too low to be visible in the linear plot of Figure 1a, but the semilogarithmic plots of Figure 1b,d show an oscillating behavior, while the time average (ideal line in the middle between the maxima and minima) followed an approximately linear behavior in the semilogarithmic scale, thus evidencing an exponential increase with time. The slope of this mean value in the semilogarithmic plot increased for voltage values from 100 to 250 V, then decreased for the 300 and 350 V values, as seen in Figure 1b,d. Moreover, the semilogarithmic plot related to the 350 V peak bias shows a deviation from linearity at about 750 ns. The oscillation amplitude appeared constant with time in the semilogarithmic scale, which means that the ratio between the adjacent maxima and minima remained approximately constant. Figure 1c shows a zoom of the first 100 ns in linear scale, evidencing more clearly the oscillating behavior. An increase in amplitude with time was observed for all signals except for the 400 V peak bias voltage, for which a slow decrease of the electron density oscillation amplitude was observed with time.

In the second regime, after about 1 μ s of simulated time for the 300 V peak bias voltage, a linear increase of the electron density with time is clearly visible in Figure 1a, appearing as an almost flat line in the semilogarithmic scales of Figure 1b,d. Moreover, the oscillation of electron density with time appears much less intense, compared with the first region. The time required for the transition between the two regimes reduced as the peak bias voltage increased from 150 to 250 V, then the transition time increased for 300 V and 350 V. For the 100 V value there was no transition up to the maximum simulated time, and for 400 V the simulation ended during the first regime. In the second regime, from 150 to 350 V the slope of the electron density linear increase rose with the peak bias voltage, as seen in Figure 1a.

3.2. Electron Mean Energy

The mean energy of the electrons is shown as a function of time in Figure 2, for peak voltages (a) in range 150–350 V, and (b) 100, 400 V. In this case, similarly to the electron density, a dramatic change of behavior was observed separating two regimes, for peak bias voltages in range 150–350 V, while for bias voltages of 100 and 400 V the first regime only was observed. In the first regime, a strongly oscillating behavior of the electron mean energy was apparent, with an approximately constant amplitude increasing with the peak bias voltage, as seen in Figure 2a,c. In the second regime the mean electron energy started to fall, in terms of both the oscillation amplitude and the mean value, eventually reaching a finale state in which the oscillation ranged between 0.7 and 1.3 V depending on the peak bias voltage; as seen in Figure 2d, reporting the last 100 ns of simulated time. The time required for the transition between the two regimes reduced as the peak bias voltage increased from 150 to 250 V, but then increased for 300 and 350 V, consistent with observations for the electron density.

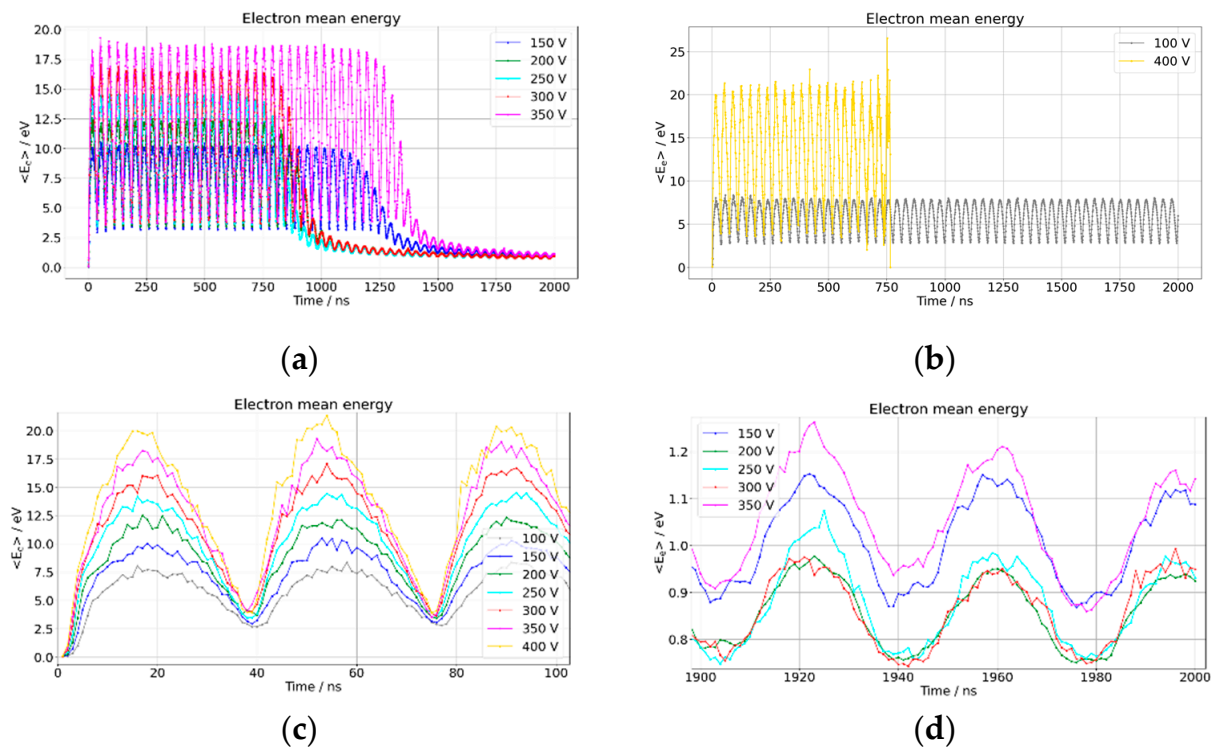


Figure 2. Time evolution of the mean electron energy during the simulation for different values of the peak bias voltage: (a) 150–350 V and (b) 100, 400 V; and for the (c) first and (d) last 100 ns of simulated time.

3.3. Debye Length

Figure 3a shows the time evolution of the Debye length (calculated from the electron density and mean energy by means of Equation (A3)) during the simulation for peak bias voltages in the range 100–400 V, in a semilogarithmic scale. Figure 3b shows a zoom of the time region up to 100 ns in a linear scale. The semilogarithmic plot shows a separation between two regimes, as already observed for the plasma density and the electron mean energy, for all the peak bias voltages except 100 and 400 V. In the first regime, an exponential decrease of λ_D with time (appearing as a linear decrease in the semilogarithmic plot) was observed, modulated by an oscillating behavior. This is to be expected, as the electron mean energy in this region of simulation time was oscillating around a constant value, while the electron density showed an exponential increase; λ_D is proportional to the square root of their ratio (Equation (A3)). The zoom on the first 100 ns shows the oscillating behavior,

the amplitude of which increased with the peak bias voltage. However, this increase was much more intense from 350 to 400 V, where we observe a doubling of the Debye length peak value.

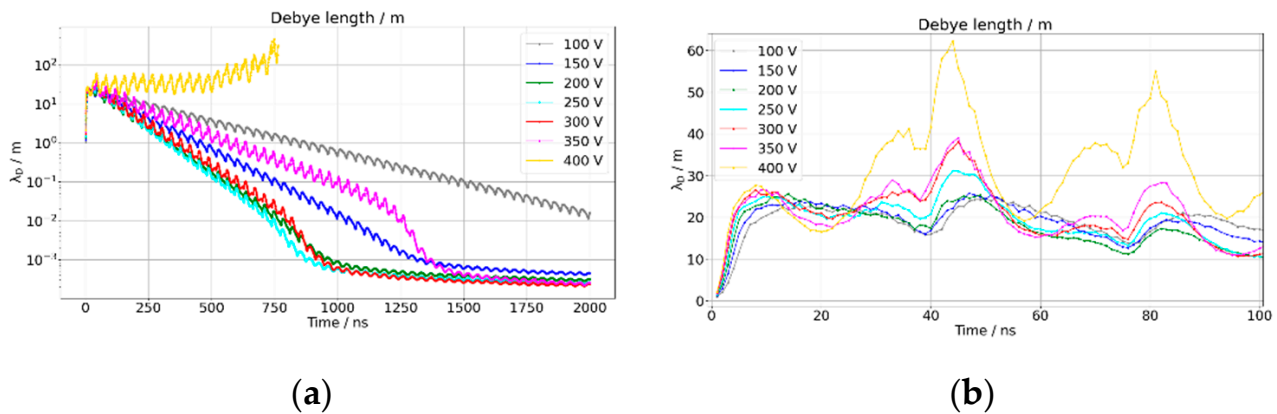


Figure 3. Time evolution of the Debye length λ_D during the simulations: (a) Semilogarithmic scale; and (b) zoom of region 0–100 ns in linear scale.

3.4. Debye Number

The time evolution of the Debye number N_D , which was calculated from the electron density and mean energy by means of Equation (A4), is shown in Figure 3 using (a) linear and (b) semilogarithmic scales. Zoomed graphs are also provided of (c) the first 100 ns in linear scale and (d) the 700–1500 ns range in semilogarithmic scale. The Debye number is commonly defined as the mean number of electrons comprised in a sphere having a radius equal to the Debye length, and values of N_D much greater than unity are usually associated with strong collective behavior of the electrons [22]. It is interesting to observe that, in the situation under consideration, the N_D value was already quite high ($N_D = 10^6$) at the beginning of the simulation, then increased by several orders of magnitude during the first half of the RF cycle, as seen in Figure 4b,c. This can be explained by the fact that the mathematical expression of N_D (Equation (A4)), depends strongly on the electron energy, which increased considerably during the first half of the RF cycle, as shown in Figure 2, and depends much less on the electron density. After this initial rise, except at the 400 V peak bias voltage, the N_D value oscillated around an exponentially decreasing mean value (appearing as decreasing linear behavior in the semilogarithmic scale), with a change of slope in the region between 750 nm and 1 μ s.

3.5. Plasma Frequency

The evolution of the plasma frequency ν_p (calculated from the electron density and mean energy by means of Equation (A5)) with the simulated time is shown in Figure 5 in (a) linear and (b) semilogarithmic scales. Zoomed graphs in semilogarithmic scale of (c) the first 100 ns in linear scale, and (d) the 700–1500 ns window (for peak bias voltages in range 150–350 V only) are also shown. The presence of two regimes is clearly visible, especially in graphs of Figure 5a,d, as well as the change of the time required for the onset of the second regime. In fact, increasing the peak bias voltage from 150 to 250 V, the regime transition shifted to shorter times, but when increasing further to 300 and 350 V, it began to shift to longer times. The first 100 ns of simulated time showed that for peak bias voltages in range 100–350 V, the amplitude of the oscillation increased with time, while for 400 V an opposite behavior was observed.

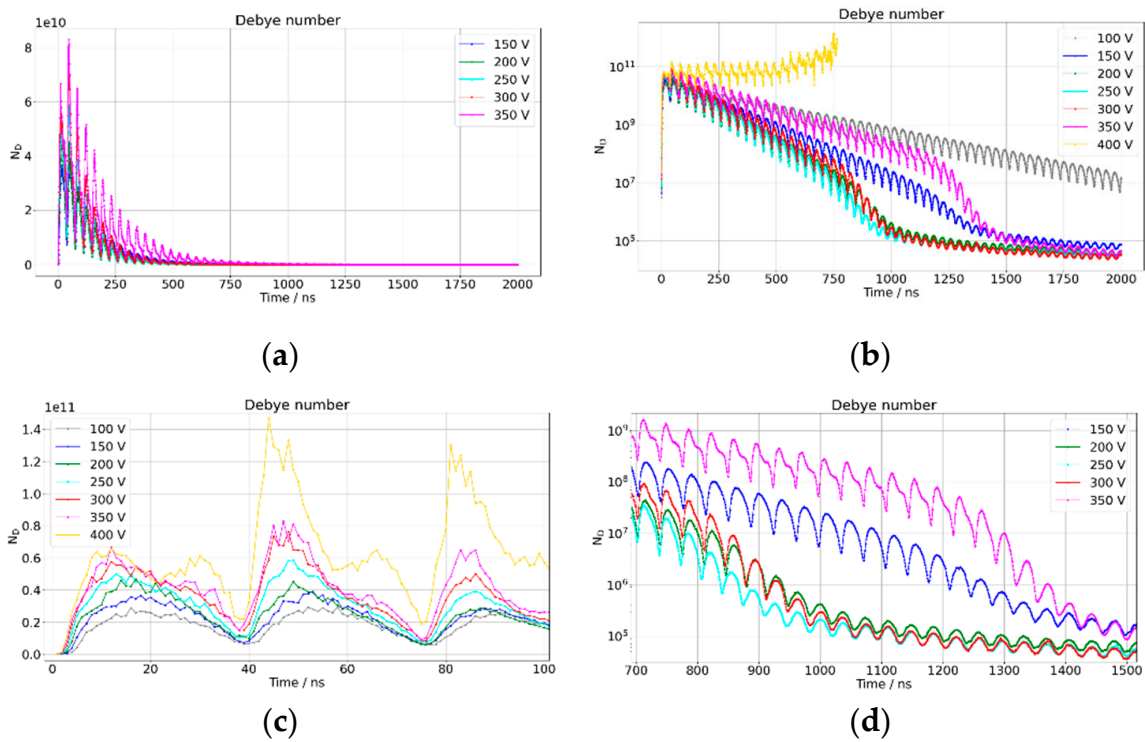


Figure 4. Time evolution of the Debye number N_D during the simulations: (a) Linear scale; (b) semilogarithmic scale; (c) zoom of region 0–100 ns in linear scale; and (d) zoom of region 700–1500 ns in semilogarithmic scale.

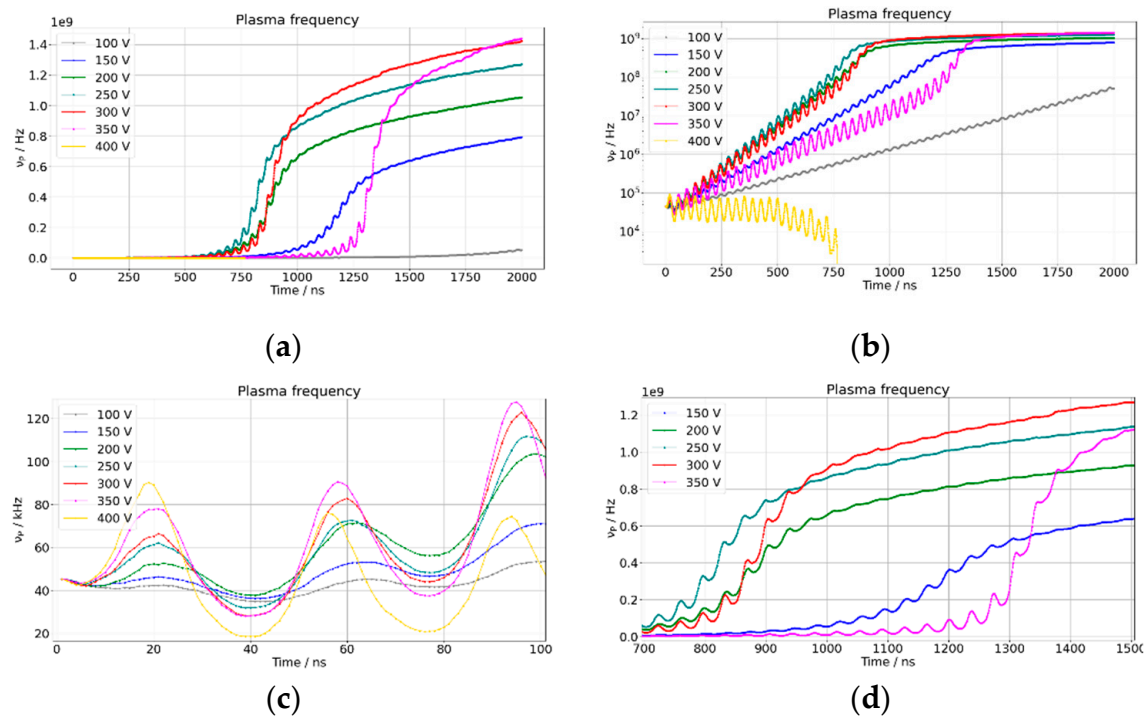


Figure 5. Time evolution of the plasma frequency ν_p during the simulations: (a) Linear scale; (b) semilogarithmic scale; (c) zoom of region 0–100 ns in linear scale; and (d) zoom of region 700–1500 ns in semilogarithmic scale, for peak bias voltages in range 150–350 V. In all the vertical scales ν_p is in Hz, except (c) where it is expressed in kHz to improve the readability.

3.6. Spatial Distribution of the Electric Potential

The spatial distributions of the bias voltage calculated at different simulation times are shown in Figures 6–8. Each plot shows the electric potential as a function of the z coordinate, which is the distance from the biased electrode along the normal direction, for the different values of the peak bias voltage. The grounded electrode was located at $z = 20$ mm and had a fixed potential of 0 V. Since the PIC method was implemented in one dimension only, the charge density, the electric potential, and the electric field were considered equal for all points sharing the same value of the z coordinate, i.e., the planar surfaces parallel to the electrodes.

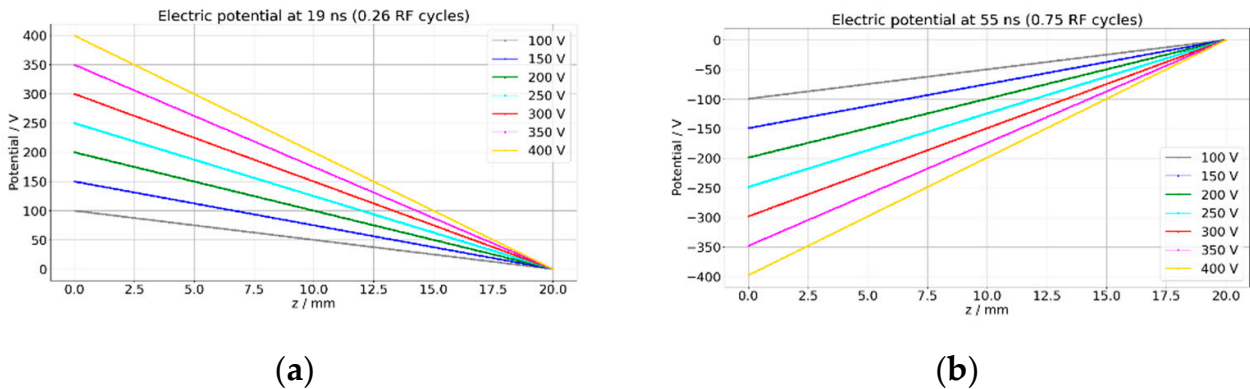


Figure 6. Spatial distribution of the electric potential along the direction normal to the electrodes, for different values of the peak bias potential during the first RF cycle, at (a) $1/4$ of RF period (positive maximum of the bias potential) and (b) $3/4$ of RF period (negative maximum of the bias potential).

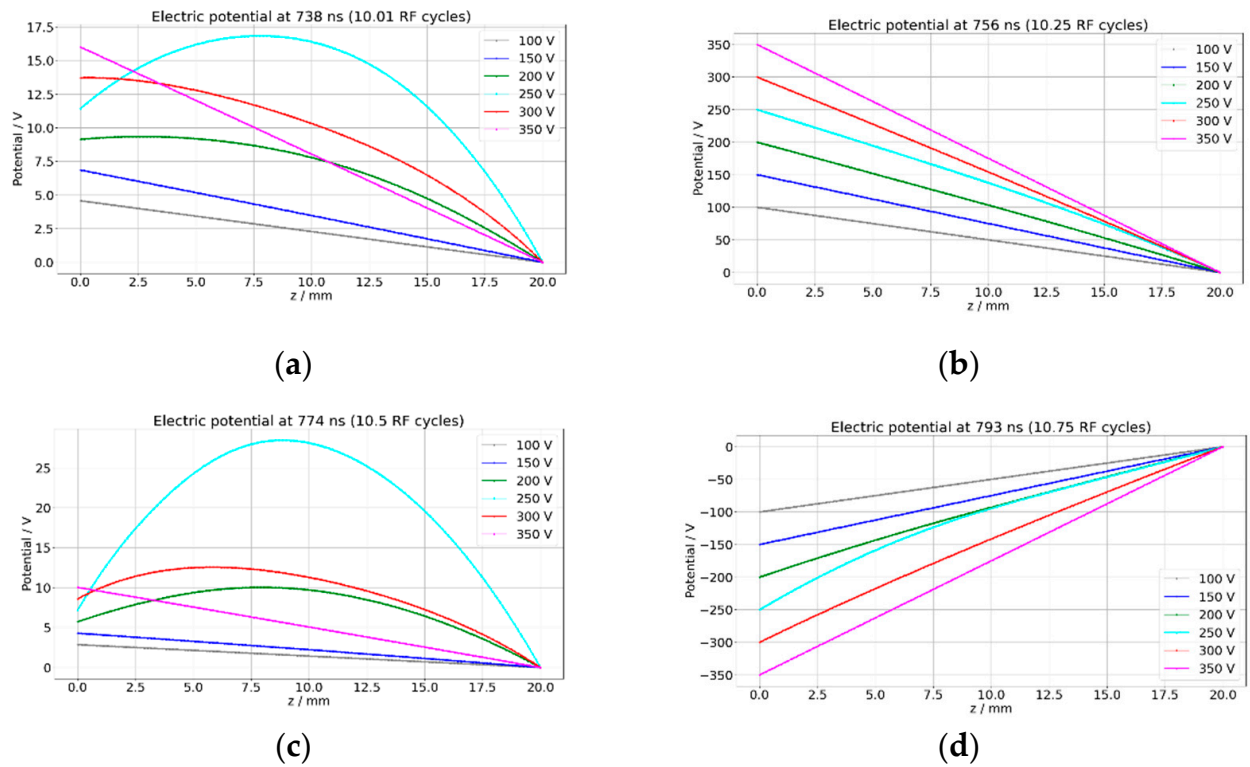


Figure 7. Spatial distribution of the electric potential along the direction normal to the electrodes, for different values of the peak bias potential during the 10th RF cycle: (a) At the beginning of the RF period (b) at $1/4$ of RF period; (c) at $1/2$ of RF period; and (d) at $3/4$ of RF period.

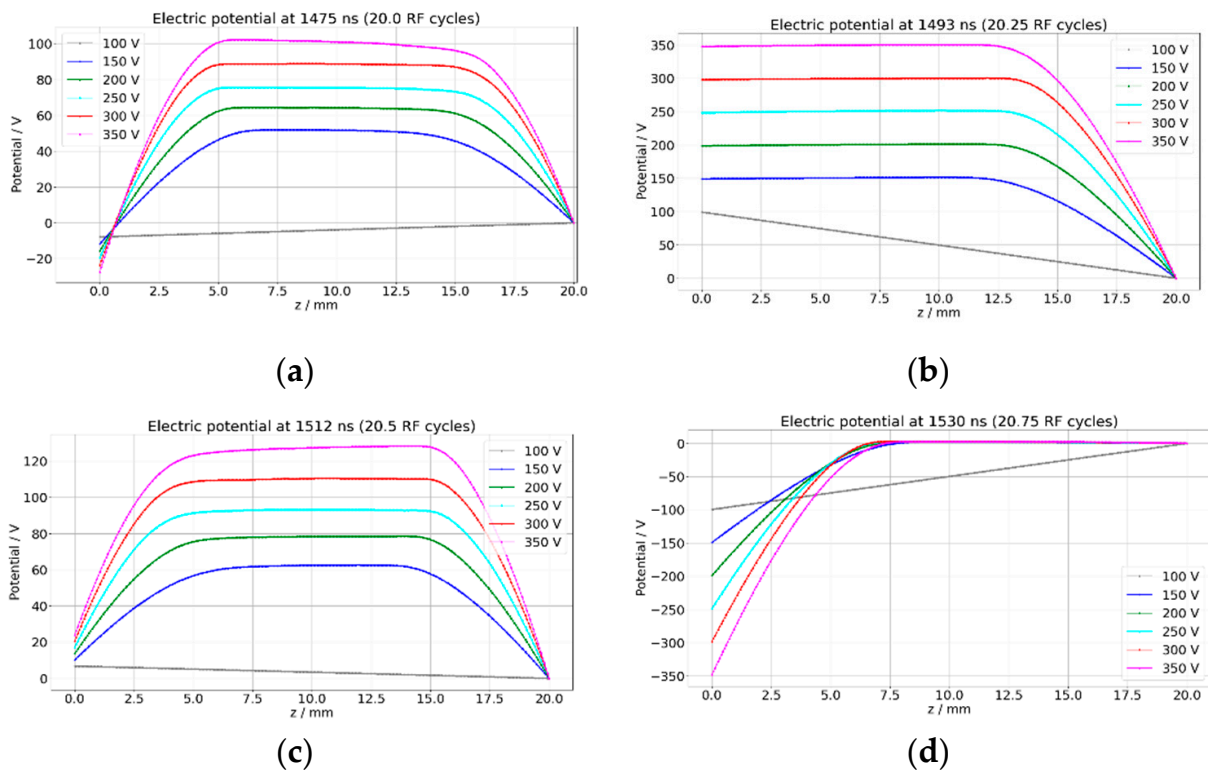


Figure 8. Spatial distribution of the electric potential along the direction normal to the electrodes, for different values of the peak bias potential during the 20th RF cycle: (a) At the beginning of the RF period (b) at 1/4 of RF period; (c) at 1/2 of RF period; and (d) at 3/4 of RF period.

Figure 6 shows the bias voltage calculated at 1/4 and 3/4 of the first RF cycle, when the electric bias on the polarized electrode reached maximum positive and maximum negative values, respectively. The absolute value of the voltage decreased from the biased electrode to the grounded one ($z = 0$ and $z = 20$ mm, respectively) with a constant slope, revealing a uniform electric field in the plasma volume. This result unsurprisingly shows that at the beginning of the simulation the charged particle density was too low to provide an effect on the electric field distribution, which was essentially dominated by the external bias.

Figure 7 shows the bias voltage calculated at the beginning, at 1/4, at 1/2, and at 3/4 of the 10th RF cycle, corresponding to the time window between 738 and 793 ns. For peak bias voltages of 100, 150, and 350 V, the potential changed linearly with z , showing a uniform electric field. Instead, for 200, 250 and 300 V, a bending of the voltage slope was clearly apparent, especially at the beginning and at 1/2 of the RF cycle (738 and 774 ns), much more pronounced for a peak bias of 250 V, showing that the charge density started to provide a contribution to the electric field of intensity comparable to the one of the external field. It is interesting to compare these results with the plots in Figure 1b,d, since the peak voltage values for which the bending is visible were those where, at the same of simulated time, the transition between the two regimes of plasma density increase had already begun to take place.

Figure 8 shows the bias voltage calculated at the beginning, at 1/4, at 1/2, and at 3/4 of the 20th RF cycle, corresponding to the time window between 1475 and 1530 ns. In this case, a bending of the voltage distribution was clearly observed for all values of peak bias voltage between 150 and 350 V, but not 100 V. If we compare again this result with the plots in Figure 1b,d, we can observe that in this time window the electron density time evolution had completed the transition from the exponential to the linear regime for all peak values except 100 V (not including 400 V, for which the time evolution had already stopped).

3.7. Electron Energy Distribution Functions

Figures 9–11 show *EEDFs* evaluated at the beginning of the 10th and the 20th RF cycles, for peak bias voltages of 150, 200, and 250 V respectively, with an inset containing a zoom of the 0–10 eV region, added in order to make the peak position more readable. Figure 9 shows that, for a peak bias voltage of 150 V, there is a small change in the *EEDF* from the 10th to the 20th RF cycle, with a shift of the peak position towards a lower energy. A more pronounced change is visible in Figure 10, for a peak bias voltage of 250 V: although the peak moves at lower energy, we can observe an increase of the high-energy tail, with an increase of the maximum electron energy. Figure 11, related to a peak bias voltage of 350 V, shows a less peaked shape of the *EEDFs* and, again, a shift of the peak towards lower energy from the 10th to the 20th RF cycle, together with an increase of the high-energy tail.

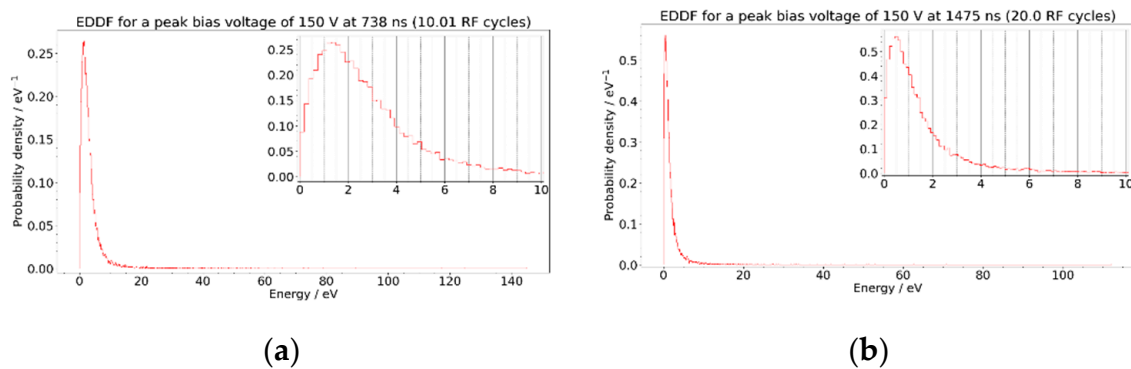


Figure 9. Electron energy distribution function for a peak bias voltage of 150 V at the beginning of: (a) the 10th RF period; and (b) the 20th RF period, the inset contains a zoom of the 0–10 eV region.

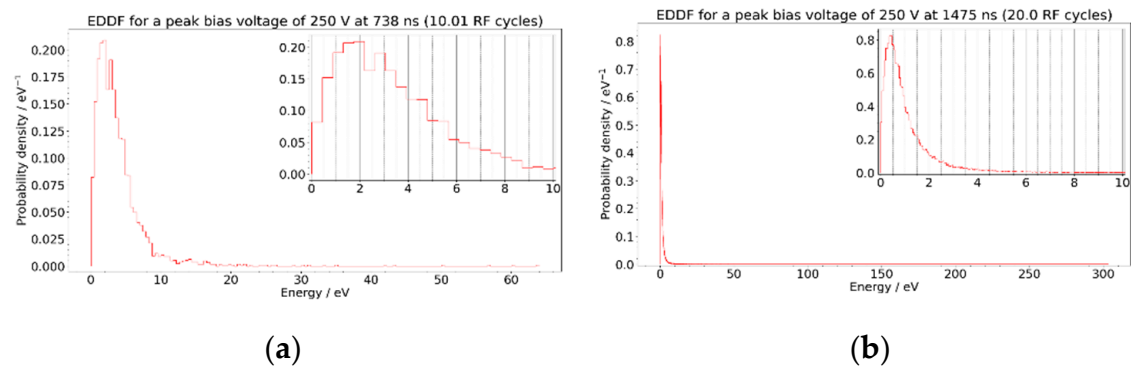


Figure 10. Electron energy distribution function for a peak bias voltage of 250 V at the beginning of: (a) the 10th RF period; and (b) the 20th RF period, the inset contains a zoom of the 0–10 eV region.

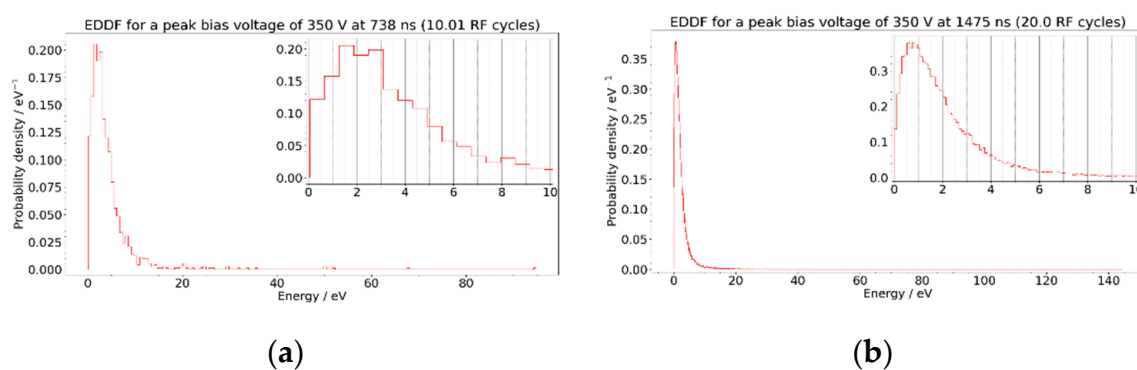


Figure 11. Electron energy distribution function for a peak bias voltage of 350 V at the beginning of: (a) the 10th RF period; and (b) the 20th RF period, the inset contains a zoom of the 0–10 eV region.

3.8. Variability of the Simulation Results

The discharge simulation for the peak voltage of 300 V was repeated 5 times to estimate the variation of the results within different runs with the same parameters. The plots of the electron density time evolution for the different simulation runs are shown in Figure 12 in linear (a) and semilogarithmic (b) scale, while the mean electron energy plots are shown in Figure 13. The variation shown by the graphs is clearly much lower than the one obtained in simulation runs when the bias peak value was varied (Figure 1a,b and Figure 2a).

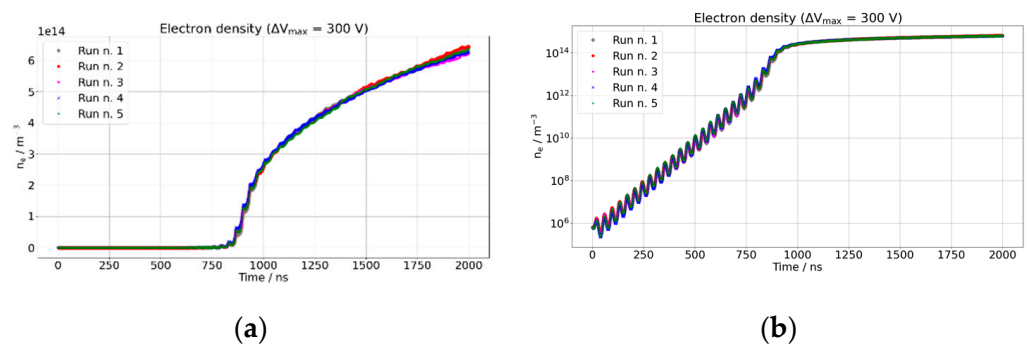


Figure 12. Time evolution of the electron density during the five simulation runs with $\Delta V_{max} = 300$ V: (a) in a linear scale; and (b) in a semilogarithmic scale.

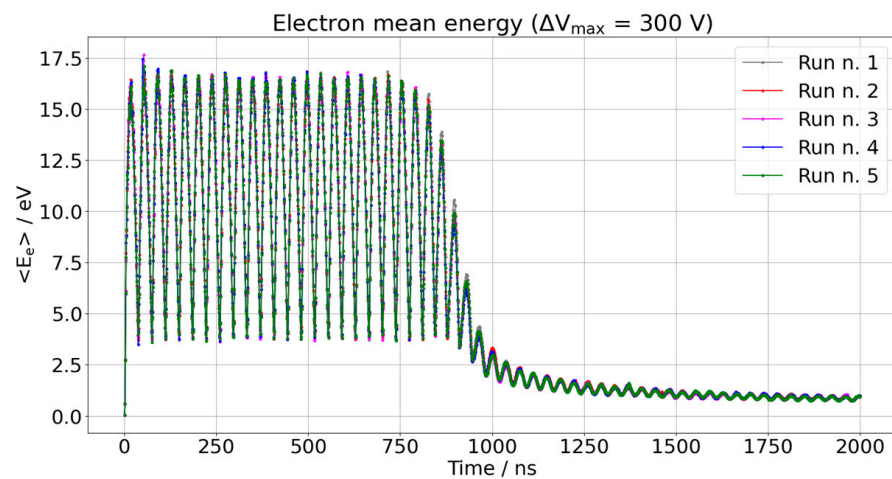


Figure 13. Time evolution of the mean electron energy during the five simulation runs with $\Delta V_{max} = 300$ V.

4. Discussion

The main goal of this work is to give a contribution to the understanding of the processes involved in the ignition mechanism of low pressure RF-CCP discharges. The most evident result obtained by these simulations is the presence, during the first discharge microsecond in the chosen discharge conditions, of a transition between two regimes, characterized by different behaviors of the plasma parameters with time. While the electron density changes from an exponential increase to a linear one (both of them modulated by oscillations), the electron mean energy changes from a strongly oscillating behavior around a constant mean value, with an amplitude depending on the peak voltage bias, to an oscillation with much lower amplitude and mean value, which is similar for all the investigated peak bias voltages.

The other plasma parameters, such as Debye length, Debye number, and plasma frequency [23], reflect these behaviors, since they are calculated starting from the electron density and mean energy, as described in Appendix B. It is interesting to note that the Debye number rises to values greater than 10^{10} already during the first half RF cycle, but

later it reduces to much lower values, especially after the transition to the second regime, which however are still greater than 10^4 . Since high values of the Debye number are usually considered associated with a collective behavior of charged particles [22], the simulation results suggest that, based on this parameter only, the charges should show a collective behavior starting from the very beginning. On the other hand, during the first RF cycle, the spatial distribution of the bias voltage does not show any sign of bending, revealing the absence of a significant self-consistent electric field, which appears with the transition between the two regimes only, as seen in Figures 6–8.

At the beginning of the simulation, the plasma frequency ν_p is in the range 40–120 kHz, about two orders of magnitude lower than the RF frequency $\nu_{RF} = 13.56$ MHz, so the electrons should not be able to provide a quick enough response to the variation of the external bias [23]. According to the results shown in Figure 5b, the transition between the two regimes is always associated with values of the plasma frequency of the order of 100 MHz, about ten times ν_{RF} . These results suggest that the plasma frequency has a role in driving the transition between the two regimes observed. In fact, as the plasma frequency rises, the difference in the behavior of electrons and ions becomes more important, since the latter have a much higher mass, that strongly limits their mobility. The transition between the two regimes seems to reflect the onset of a charge accumulation, which is associated with the development of an internal electric field, as seen in Figures 6–8. The strong reduction of the electron mean energy in the second regime could be explained considering that a considerable fraction of the energy, that in the first regime is accumulated in the electron kinetic energy, is transferred in the internal electric field developed by the charge separation.

The formation of a self-consistent electric field is observed during the 10th RF cycle, for the 200, 250 and 300 V RF amplitudes, by the bending of the voltage spatial distributions shown in Figure 7. For these values of the peak bias voltage, the transition between the two regimes happens between 800 and 900 ns, as is visible in Figure 1b,d, so the deformation of the potential distribution seems to be somehow predictive of the transition. The presence of a non uniform electric field can be associated with the development of a spatial charge, which is typically a result of the difference between the behavior of ions and electrons in the discharge [19,22]. In fact, due their higher mass, ions are much less able to follow the electric field variation, compared to electrons, and this difference leads to the accumulation of positive charges in the central region of the discharge. As the electron and ion density rise, the intensity of the electric field produced by this charge accumulation increases, eventually becoming comparable to the external one, thus producing a deformation of the potential spatial distribution.

The time required for the transition between the two regimes shows an interesting behavior, since it reduces as the peak bias voltage ΔV_{max} is risen from 100 to 250 V, but it increases when a further rise of ΔV_{max} to 300 and 350 V is applied, as is clearly visible in Figure 1a. Moreover, at 400 V no increase is observed at all and, after a few RF cycles, the simulation shows a decrease of the electron density towards zero. The same consideration applies to the slope of the electron density rise in the semilogarithmic plots of Figure 1b,d. This behavior may seem inconsistent, since, in the first regime, the amplitude of the mean electron energy oscillations increases considerably with the peak bias voltage, reaching a value as high as 20 eV for 400 V. Since the efficiency of the electron-impact ionization processes of Ar increases with the electron energy up to about 100 eV [20], one could expect the higher values of the mean electron energy to be always associated with a more rapid increase of the electron density.

A possible explanation of this behavior could be related to the time required for the electrons to move between the electrodes. In fact, a free electron produced in the discharge can contribute to the ionization processes while it is accelerated toward the electrode that, at that time, has the higher electric potential. During an half RF period, it is always accelerated toward the same electrode, since the electric field is changing in intensity, but not in direction. Obviously, a stronger electric field produces a higher electron speed,

increasing the ionization efficiency (at least up to energies of about 100 eV). However, if the electron becomes too fast, it may reach the electrode before the electric field direction changes, being removed from the discharge. Instead, if the electric field inversion happens before the electron has been absorbed, it starts to be accelerated in the opposite direction, and may not be removed from the discharge, continuing to contribute to the ionization processes. For these reasons, an excessive electron energy, and consequently speed, could increase the probability that an electron is absorbed before the inversion of the electric field takes place. As an example, considering the peak bias voltage of 350 V, the electron mean energy averaged over the first half RF cycle (1–37 ns) is 11.9 eV, which gives a time to move between the two electrodes of about 9.8 ns, which is about 26% of an half RF cycle ($\tau_{RF}/2 = 37$ ns). Since a certain fraction of the electrons has an energy higher than the mean value, as can be seen in the *EEDF* reported in Figures 9–11, there is a considerable number of them that has a high probability of being absorbed by the electrodes.

The previous considerations could explain why, in the second regime observed, the slope of the linear electron density always rises with the peak bias voltage, as seen in Figure 1a, for 300 V and 350 V also. In fact, after the transition between the two regimes has been completed, the amplitude and mean value of the $\langle E_e \rangle$ oscillations drop dramatically, as seen in Figure 2a,d. Considering again a 350 V peak bias voltage, the value of $\langle E_e \rangle$ averaged over the last simulated half RF cycle (1954–1991 ns) is 1 eV, corresponding to a time required to move between the electrodes of 33.7 ns, about 91% of an half RF cycle. It is possible to presume that, in these conditions, the number of electrons that are removed from the discharge by electrode absorption is much lower compared to the situation of the first regime.

As an additional consideration, the onset of a charge separation is usually associated with the formation of sheath structures near the electrodes, and the electric potential distribution shown in Figure 8 seems to confirm the sheaths presence, with the formation of potential barriers at both the electrodes. These may prevent the electrons with energy lower than a certain threshold from reaching the electrodes, thus avoiding their absorption. Since this kind of structure is not present in the potential distribution during the first regime (Figures 6 and 7), it could be considered as an additional mechanism increasing the lifetime of electrons in the discharge during the second regime.

5. Conclusions

Within the limits of the model used, the simulation of the first 2 μ s of a low pressure (66.6 Pa) Ar RF-CCP discharge with peak bias voltages in range 100–400 V showed the presence of two regimes, characterized by an exponential and linear increase of the electron density with time, respectively. The behavior of the electron mean energy changes also considerably between the two regimes: while in the first one it shows oscillations with peak values that reach 20 eV for 400 V peak bias voltage, in the second regime the oscillations are strongly reduced in both amplitude and mean value, which becomes of the order of 1 eV. The time required for the transition between the two regimes is reduced with the peak bias voltage rise up to 250 V, but increasing it further to 300 and 350 V produces the opposite effect, and for 400 V there is no transition at all.

Funding: This research received no external funding.

Data Availability Statement: The data presented in this study are available in the article.

Conflicts of Interest: The author declares no conflict of interest.

Appendix A. Description of the CCPLA Software

CCPLA is a script for the simulation of capacitively coupled plasma discharges, which is part of the *pysica* project, freely downloadable from the *pypi* [24] repository under GPL license [25]. The software is developed in Python for the parts related to the import-export of data, graphical output and GUI, and in Fortran for the parts related to the numerical

calculations involved in the simulation. The Fortran part is compiled as a Python module, using the F2Py software [26] and the the GNU Fortran compiler [27].

The software is designed to simulate a gas discharge in the volume comprised between two parallel square electrodes, between which a DC or RF signal is applied, an inside which a gas or gas mixture at low pressure is comprised. It uses a 1d-3v (1 dimension for the particle positions and 3 dimensions for the particle speed) electrostatic PIC-MCC (particle in cell with montecarlo collisions) model.

The required input data are:

- geometrical characteristics of the discharge: electrodes lateral size and distance between them;
- characteristics of the sinusoidal electric signal applied to the electrodes: peak voltage amplitude, frequency and initial phase;
- simulation time step, time between data acquisition, and requested simulated time;
- tabulated cross section values for the collision processes considered in the simulation.

The following output data, are shown as text output and as runtime graphs, and can be saved on files, with a periodicity chosen by the user:

- electric current flowing between the electrodes;
- electric potential distribution along the axis normal to the electrodes;
- electron number density;
- electron energy: mean, maximum, minimum values, and standard deviation;
- angle between electron velocity vector and electric field direction: mean, maximum, minimum values, and standard deviation;
- electron energy distribution function;
- ion energy distribution function.

The following data are also available, for molecular gases only:

- dissociation rate;
- dissociation rate constant.

Appendix A.1. Simulation Modules

The Fortran-compiled Python module is divided in different Fortran modules, each one responsible for a different step of the simulation process:

- *PIC module*: calculation of the electric potential, electric field, and particle acceleration components, using the particle-in-cell scheme in one dimension (normal to the electrodes surfaces);
- *particle mover*: calculates the new velocity components and positions of electrons and ions at each time step, using the leap-frog scheme, on the basis of the acceleration computed by the PIC module;
- *collision manager*: checks which particles experienced a collision, using a montecarlo method, and manages the collision effects, such as changing particles velocities and creating a list of particles to add or remove;
- *particle manager*: adds the electrons and ions produced by the ionization events, removes the particles that reached the electrodes and manages the variable weights.

It is important to remark that the pseudorandom number sequence is restarted, and seed of the pseudorandom number generator is changed, at each call of the Fortran module, which, in the present case, means every 1 ns of simulated time. To improve randomness, the seed is calculated on the basis of the state of the internal system clock.

Appendix A.2. PIC Module

The software implements a 1D PIC model, generating one dimensional cells in the direction parallel to the electric field (z axis). This means that all the physical quantities, such as charge density, electric potential, as well as electric field intensity, are considered

uniform along the directions parallel to the electrodes surfaces (x and y axes), and their variation is considered along the z axis only.

The charge density is calculated at the cell boundaries on the basis of the position of the electrons and ions in the z direction, then the electric potential is obtained by solving the one-dimensional, discretized Poisson equation [19,28]. The electric field intensity acting on each computational particle, as well as its acceleration along the z axis direction, are then calculated.

The PIC module is the most computational intensive part of the software, and the development of a parallelized version of it is planned for future versions.

Appendix A.3. Particle Mover

The electron and ion motion is actuated following the leap-frog method [19,28], in which the speeds and positions are calculated at times shifted by $\Delta t/2$, where Δt is the simulation time step [19,28].

Appendix A.4. Collision Manager

The collision processes that were considered in the simulation are listed in Table 3. For the electron-Ar collisions the Ar atoms were considered at rest, due to large difference between the electron and atom speeds, whereas for the collisions between the Ar ions and atoms, both particles were considered moving, and the collision probability was calculated in their center of mass frame of reference. Electron-ion Coulomb collisions were not taken into account, since they are usually considered negligible for electron and ion densities up to 10^{18} m^{-3} [19]. The probability of a collision of an electron or ion with a neutral particle during the time step Δt is given by the following expression [19,28]:

$$p_{coll} = 1 - e^{-n_{gas}\sigma_{tot}v_{rel}\Delta t} \quad (\text{A1})$$

where n_{gas} is the density of neutral atoms or molecules (Ar atoms in the case of the present work), σ_{tot} is total cross section for collisions with neutrals, and v_{rel} is the relative speed of the electron or ion respect to the neutral particle. In the case of electrons only, v_{rel} was considered equal to the electron speed, due to the big difference between electron and neutral speeds.

Appendix A.5. Particle Manager

The computational electrons and ions are removed from the simulation when they reach one of the electrodes. The software configuration allows to choose whether the particles that reach the lateral border of the discharge are removed or re-enter on the opposite side: in the case of the present work the latter choice has been made, since with the chosen pressure the mean free path is much shorter than the electrode lateral dimensions. Electron-ion recombination processes are not taken into account, since they are very rare at the simulated electron and ion number densities [19]. Separate computational weights are used for electrons and ions, and they are increased during the simulation, as the number of computational particles is raised by the ionization processes. An example of the increase of the electron weight with the simulated time is shown in Figure A1. Each time the weight is increased, a statistically neutral sample is extracted from the population of the computational electrons or ions.

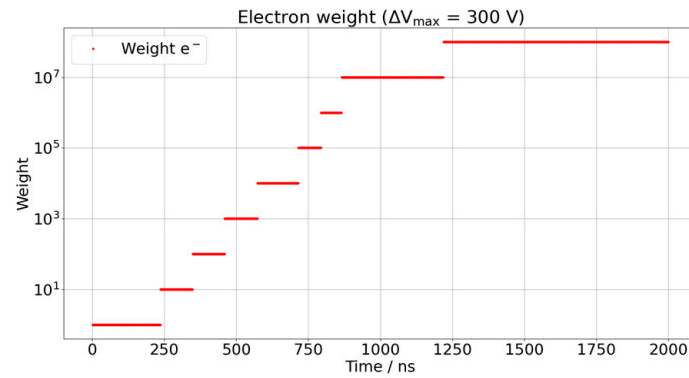


Figure A1. Time evolution of the electron weight during a simulation run with a maximum peak voltage $\Delta V_{max} = 300$ V.

Appendix B. Methods Used to Calculate the Plasma Parameters

The Debye length λ_D is defined as the minimum distance over which the condition of quasineutrality (approximately equal number of positive and negative charges) is granted, and is given by the following expression [22]:

$$\lambda_D = \sqrt{\frac{\epsilon_0 k_B T_e}{e^2 n_e}} \tag{A2}$$

where ϵ_0 is the vacuum permittivity, e is the electron charge, k_B is the Boltzmann constant, n_e is the electron density, and T_e is the electron temperature expressed in kelvin. If we approximate the electron energy distribution function to be Maxwellian, so that the electron mean energy is $\langle E_e \rangle = 3/2 k_B T_e$ we can express λ_D as a function of $\langle E_e \rangle$ and n_e :

$$\lambda_D = \sqrt{\frac{2 \epsilon_0 \langle E_e \rangle}{3 e^2 n_e}} = A \sqrt{\frac{\langle E_e \rangle}{n_e}} \tag{A3}$$

where $A \simeq 1.51 \times 10^{13} \text{ J}^{-1/2} \text{ m}^{-1/2}$ is a constant.

The Debye number is usually defined as the mean number of electrons comprised inside a sphere having a radius equal to the Debye length λ_D [22]. Once calculated the Debye length, N_D can be obtained by multiplying the volume of a sphere having radius equal to λ_D by the electron density:

$$N_D = \frac{4}{3} \pi \lambda_D^3 n_e = \frac{4}{3} \pi A^3 \sqrt{\frac{\langle E_e \rangle^3}{n_e}} = B \sqrt{\frac{\langle E_e \rangle^3}{n_e}} \tag{A4}$$

where $B \simeq 1.46 \times 10^{40} \text{ J}^{-3/2} \text{ m}^{-3/2}$ is another constant.

The plasma frequency ν_P can be considered as the maximum frequency of an external electric field to which the electrons are able to respond, moving quickly enough to preserve quasineutrality. It depends on the electron density only, and can be obtained by the following Equation [22]:

$$\nu_P = \sqrt{\frac{e^2 n_e}{\epsilon_0 m_e}} = C \sqrt{n_e} \tag{A5}$$

where m_e is the electron mass and $C \simeq 56.4 \text{ m}^{3/2} \text{ s}^{-1}$ is a constant.

References

1. Chabert, P.; Tsankov, T.V.; Czarnetzki, U. Foundations of capacitive and inductive radio-frequency discharges. *Plasma Sources Sci. Technol.* **2021**, *30*, 024001. [CrossRef]
2. Ostrikov, K.; Xu, S.; Huang, S.Y.; Levchenko, I. Nanoscale surface and interface engineering: Why plasma-aided? *Surf. Coat. Tech.* **2008**, *202*, 5314–5318. [CrossRef]
3. Marchack, N.; Buzi, L.; Farmer, D.B.; Miyazoe, H.; Papalia, J.M.; Yan, H.; Totir, G.; Engelmann, S.U. Plasma processing for advanced microelectronics beyond CMOS. *J. Appl. Phys.* **2021**, *130*, 080901. [CrossRef]
4. Xiao, S.Q.; Xu, S.; Ostrikov, K. Low-temperature plasma processing for Si photovoltaics. *Mat. Sci. Eng. R* **2014**, *78*, 1–29. [CrossRef]
5. Granqvist, C.G. Electrochromics for smart windows: Oxide-based thin films and devices. *Thin Solid Film.* **2014**, *564*, 1–38. [CrossRef]
6. Hammer, T. Atmospheric Pressure Plasma Application for Pollution Control in Industrial Processes. *Contrib. Plasma Phys.* **2014**, *54*, 187–201. [CrossRef]
7. Vasudev, M.C.; Anderson, K.D.; Bunning, T.J.; Tsukruk, V.V.; Naik, R.R. Exploration of Plasma-Enhanced Chemical Vapor Deposition as a Method for Thin-Film Fabrication with Biological Applications. *ACS Appl. Mater. Interfaces* **2013**, *5*, 3983–3994. [CrossRef]
8. Weltmann, K.D.; von Woedtke, T. Plasma medicine-current state of research. *Plasma Phys. Control. Fusion* **2017**, *59*, 014031. [CrossRef]
9. Cha, S.; Park, Y.-S. Plasma in dentistry. *Clin. Plasma Med.* **2014**, *2*, 4–10. [CrossRef]
10. Wang, X.-Y.; Liu, J.-R.; Liu, Y.-X.; Donko, Z.; Zhang, Q.-Z.; Zhao, K.; Schulze, J.; Wang, Y.N. Comprehensive understanding of the ignition process of a pulsed capacitively coupled radio frequency discharge: The effect of power-off duration. *Plasma Sources Sci. Technol.* **2021**, *30*, 075011. [CrossRef]
11. Ma, F.-F.; Zhang, Q.-Z.; Schulze, J.; Sun, J.-Y.; Wang, Y.-N. Temporal evolution of plasma characteristics in synchronized dual-level RF pulsed capacitively coupled discharge. *Plasma Sources Sci. Technol.* **2021**, *30*, 105018. [CrossRef]
12. Su, Z.-X.; Shi, D.-H.; Liu, Y.-X.; Zhao, K.; Gao, F.; Wang, Y.-N. Radially-dependent ignition process of a pulsed capacitively coupled RF argon plasma over 300 mm-diameter electrodes: Multi-fold experimental diagnostics. *Plasma Sources Sci. Technol.* **2021**, *30*, 125013. [CrossRef]
13. Darnon, M.; Cunge, G.; Braithwaite, N.J. Time-resolved ion flux, electron temperature and plasma density measurements in a pulsed Ar plasma using a capacitively coupled planar probe. *Plasma Sources Sci. Technol.* **2014**, *23*, 025002. [CrossRef]
14. Denysenko, I.B.; von Wahl, E.; Mikikian, M.; Berndt, J.; Ivko, S.; Kersten, H.; Kovacevic, E.; Azarenkov, D.M.; Cunge, G.; Braithwaite, N.J. Plasma properties as function of time in Ar/C₂H₂ dust-forming plasma. *J. Phys. D Appl. Phys.* **2020**, *53*, 135203. [CrossRef]
15. Schulze, J.; Derzsi, A.; Dittmann, K.; Hemke, T.; Meichsner, J.; Donko, Z. Ionization by Drift and Ambipolar Electric Fields in Electronegative Capacitive Radio Frequency Plasmas. *Phys. Rev. Lett.* **2011**, *107*, 275001. [CrossRef]
16. Schmidt, N.; Schulze, J.; Schungel, E.; Czarnetzki, U. Effect of structured electrodes on heating and plasma uniformity in capacitive discharges. *J. Phys. D Appl. Phys.* **2013**, *46*, 505202. [CrossRef]
17. Behounek, F.; Kletschka, J.A. Ionization of Air in an Air-conditioned Building. *Nature* **1938**, *142*, 956. [CrossRef]
18. Suchanowski, A.; Wiszniewski, A. Changes in Ion Concentration in the Air during the Breathing Process of a Human Being. *Pol. J. Environ. Stud.* **1999**, *8*, 259–263.
19. Donkó, Z.; Derzsi, A.; Máté Vass, M.; Horváth, B.; Wilczek, S.; Hartmann, B.; Hartmann, P. eduPIC: An introductory particle based code for radio-frequency plasma simulation. *Plasma Sources Sci. Technol.* **2021**, *30*, 095017. [CrossRef]
20. Raju, G.G. Electron-atom Collision Cross Sections in Argon: An Analysis and Comments. *IEEE Trans. Dielectr. Electr. Insul.* **2004**, *11*, 649–673. [CrossRef]
21. Bogaerts, A.; Van Straaten, M.; Gijbel, R. Monte Carlo simulation of an analytical glow discharge: Motion of electrons, ions and fast neutrals in the cathode dark space. *Spectrochim. Acta* **1995**, *50B*, 179–196. [CrossRef]
22. Schumacher, U. Basics of Plasma Physics. In *Lecture Notes in Physics-Plasma Physics*; Dinklage, A., Klinger, T., Marx, G., Schweikhard, L., Eds.; Springer: Berlin/Heidelberg, Germany, 2005; pp. 3–20.
23. Von Keudell, A.; Schulz-von der Gathen, V. Foundations of low-temperature plasma physics-an introduction. *Plasma Sources Sci. Technol.* **2017**, *26*, 113001. [CrossRef]
24. Pysica 0.2.0. Available online: <https://pypi.org/project/pysica> (accessed on 15 August 2022).
25. GNU General Public License. Available online: <https://www.gnu.org/licenses/gpl-3.0.html> (accessed on 14 August 2022).
26. Peterson, P. F2PY: A tool for connecting Fortran and Python programs. *Int. J. Comput. Sci. Eng.* **2009**, *4*, 296–305. [CrossRef]
27. The GNU Fortran Compiler. Available online: <https://gcc.gnu.org/onlinedocs/gfortran> (accessed on 14 August 2022).
28. Birdsall, C.K. Particle-in-Cell Charged-Particle Simulations, Plus Monte Carlo Collisions With Neutral Atoms, PC-MCC. *IEEE Trans. Sci.* **1991**, *19*, 65–85.